Monthly Notices of the ROYAL ASTRONOMICAL SOCIETY

MNRAS **499,** 3085–3093 (2020) doi:10.1093/mnras/staa3033
Advance Access publication 2020 October 1

A pilot search for extragalactic OH absorption with FAST

Zheng Zheng,[1★] Di Li,[1,2,3★] Elaine M. Sadler,[4,5,6] James R. Allison[6,7] and Ningyu Tang[1]

[1]*National Astronomical Observatories, Chinese Academy of Sciences, 20A Datun Road, Chaoyang District, Beijing 100101, China*
[2]*University of Chinese Academy of Sciences, Beijing 100049, China*
[3]*NAOC-UKZN Computational Astrophysics Centre, University of KwaZulu-Natal, Durban 4000, South Africa*
[4]*Sydney Institute for Astronomy, School of Physics, University of Sydney, NSW 2006, Australia*
[5]*ATNF, CSIRO Astronomy and Space Science, PO Box 76, Epping, NSW 1710, Australia*
[6]*ARC Centre of Excellence for All Sky Astrophysics in 3 Dimensions (ASTRO 3D)*
[7]*Department of Physics, University of Oxford, Denys Wilkinson Building, Keble Rd., Oxford OX1 3RH, UK*

Accepted 2020 September 29. Received 2020 September 28; in original form 2020 September 1

ABSTRACT

OH absorption is currently the only viable way to detect OH molecules in non-masing galaxies at cosmological distances. There have been only six such detections at $z > 0.05$ to date and so it is hard to put a statistically robust constraint on OH column densities in distant galaxies. We carried out a pilot OH absorption survey towards eight associated and one intervening H I 21-cm absorbers using the Five-hundred-meter Aperture Spherical radio Telescope (FAST). We were able to constrain the OH abundance relative to H I ([OH]/[H I]) to be lower than $10^{-6} \sim 10^{-8}$ for redshifts z$\in$ [0.1919, 0.2241]. Although no individual detection was made, stacking three associated absorbers free of RFI provides a sensitive OH column density 3σ upper-limit $\sim 1.57 \times 10^{14}(T_x^{\rm OH}/10\,{\rm K})(1/f_{\rm c}^{\rm OH}){\rm cm}^{-2}$, which corresponds to a [OH]/[H I] $< 5.45 \times 10^{-8}$. Combining with archival data, we show that associated absorbers have a slightly lower OH abundance than intervening absorbers. Our results are consistent with a trend of decreasing OH abundance with decreasing redshift.

Key words: ISM: abundances – galaxies: evolution – galaxies: ISM – quasars: absorption lines – radio lines: galaxies – radio lines: ISM.

1 INTRODUCTION

The hydroxyl radical (OH) is one of the most widely distributed molecules in the interstellar medium (ISM) of our Galaxy (e.g. Turner 1979; Allen, Hogg & Engelke 2015; Li et al. 2018b). As an abundant simple hydride, OH was the first molecule to be detected in the radio band (Weinreb et al. 1963) and is expected to trace the total amount of H_2 before all carbon is locked into CO (van Dishoeck & Black 1988).

Galactic studies (Li et al. 2018b; Nguyen et al. 2018) show that OH traces H_2 better than CO in a substantially bigger fraction of the ISM volume, but the normal thermolized OH needs to be detected through absorption due to its excitation conditions. These results are consistent with the analysis of diffuse gamma-ray emission from Fermi (Remy et al. 2017), which also revealed wide-spread molecular gas that cannot be traced by CO, thus dubbed 'dark' molecular gas (DMG; Grenier, Casandjian & Terrier 2005).

Deep CO observations (e.g. Tacconi, Genzel & Sternberg 2020, and references therein) show that dense molecular content decreases since redshift $z \sim 1.4$. Detections of OH lines in galaxies at cosmological distances can provide further constraints on both DMG fractions of these galaxies (e.g. Gupta et al. 2018) and changes in fundamental constants at cosmological distances (e.g. Curran, Kanekar & Darling 2004; Kanekar et al. 2005, 2012; Kanekar, Ghosh & Chengalur 2018). The inferred molecular gas fraction is also important for understanding star formation rate and galaxy evolution, e.g. why the star formation rate has decreased by a factor of ∼10 since $z = 2$ (Madau & Dickinson 2014). However, there have been only six OH absorbers at cosmological distances detected up to date. Four of these detections are intervening absorbers: B0218+357 (Kanekar et al. 2003), G0248+430 (Gupta et al. 2018), PKS 1830−211 (Chengalur, de Bruyn & Narasimha 1999; Allison et al. 2017; Gupta et al. 2020), and PMN J0134−0931 (Kanekar & Briggs 2003; Kanekar et al. 2005). The other two are associated absorbers within quasars: B3 1504+377 and PKS 1413+135 (Kanekar & Chengalur 2002). Details about these detections are listed in Table 1.

Most of these OH absorbers show an OH column density about the order of $10^{15}\,{\rm cm}^{-2}$. Gupta et al. (2018) show that galaxies with $z < 0.4$ could have much lower OH column densities, i.e. below $10^{14}\,{\rm cm}^{-2}$, using a detected OH absorber and upper limits of eight non-detections and assuming the OH excitation temperature $T_x^{\rm OH} = 3.5$ K, however, a more commonly used $T_x^{\rm OH}$ for OH absorbers at cosmological distances is 10 K (e.g. Kanekar & Chengalur 2002; Kanekar et al. 2003; Curran et al. 2011). The Gupta et al. (2018) sample contains only intervening absorbers with relatively low redshifts. Grasha et al. (2020) searched 11 intervening and five associated H I absorbers for OH absorptions and report no new detections except for a re-detection of the 1667 MHz OH absorption towards PKS 1830−211. Grasha et al. (2019) searched a large sample of compact radio sources for associated H I and OH absorptions but only six of them, which have relatively larger redshifts ($z \sim 0.6$), have H I absorption detections and none of them have OH absorption detection. Intervening absorbers are mostly from foreground galaxies

★ E-mail: zz@bao.ac.cn (ZZ); dili@nao.cas.cn (DL)

Table 1. Previously detected OH absorbers at cosmological distances.

Source name	Type	z_{abs}	$\tau_{\rm H\,I,\,peak}$	$\int\tau_{\rm H\,I}\,dv$ (km s^{-1})	H I FWHM (km s^{-1})	N(H I) (10^{20} cm^{-2})	$\tau_{1667,\rm peak}$ (10^{-2})	$\int\tau_{1667}\,dv$ (km s^{-1})	N(OH) (10^{15} cm^{-2})	Refs
	(1)	(2)	(3)	(4)	(5)	(6)	(7)	(8)	(9)	(10)
PKS 1830−211	I	0.88582	0.055	5.8	96	31.72	0.7	1.83	11.39[b]	C99,KC02
B0218+357	I	0.68468	0.05	2.94	55	5.35	1	0.40	2.24	K03,KB03,C03
B3 1504+377	A	0.67343	0.32	21	62	51.73	0.83	0.448	2.18	C97,KC02
PKS 1413+135	A	0.24671	0.34	7.13	18	194.97	0.49	0.023	1.17	C92,KC02
PMN J0134−0931	I	0.7645	0.047	7.06	142	25.74	1.8	2.19[c]	4.9	KB03,K12
G0248+430	I	0.0519	0.02	0.43	20	0.55	0.4	0.08	0.063	G18

Notes. Columns: (1) Absorber type, I for intervening and A for associated. (2) Redshift of the absorber. (3) H I peak optical depth, calculated using $1.06\int\tau_{\rm H\,I}dv$ divided by the H I 21-cm absorption full width at half-maximum (FWHM; Allison et al. 2013) if not provided by the references. (4) Integrated H I optical depth. (5) H I 21-cm absorption FWHM, calculated using $1.06\int\tau_{\rm H\,I}dv/\tau_{\rm H\,I,\,peak}$ (Allison et al. 2013) if not provided by the references. (6) H I column density. The H I excitation temperatures and covering factors used in the calculations are from the listed references. They are $T_x^{\rm HI}=100$, 100, 100, 150, 200, 70 K; $f_c^{\rm HI}=0.33$, 1, 0.74, 0.1, 1, 1, respectively. (7) OH 1667 MHz line peak optical depth. (8) Integrated OH 1667 MHz line optical depth. (9) OH column density. The OH excitation temperatures and covering factors used in the calculations are from the listed references. All OH excitation temperatures are 10 K except for G2048+430, which has $T_x^{\rm OH}=3.5$ K. The OH covering factors are $f_c^{\rm OH}=0.36$, 0.4, 0.46, 0.044, 1, 1, respectively. (10) References: C99: Chengalur et al. (1999); KC02: Kanekar & Chengalur (2002); K03: Kanekar et al. (2003); C03: Cohen, Lawrence & Blandford (2003); C97: Carilli et al. (1997); KC02: Kanekar & Chengalur (2002); C92: Carilli, Perlman & Stocke (1992); KB03: Kanekar & Briggs (2003); K12: Kanekar et al. (2012); G18: Gupta et al. (2018).
Notes: (*a*) Redshift of the background QSO is from SIMBAD Astronomical Database (Wenger et al. 2000) and Barkhouse & Hall (2001). (*b*) This value is from KC02 that used the parameters listed above. Gupta et al. (2020) derived a lower OH column density, 1.46×10^{15}cm^{-2}, using the data from the MeerKAT-64 array with a lower $T_x^{\rm OH}=5.14$ K and a higher $f_c^{\rm OH}=1$. (*c*) Estimated using the Gaussian fitting parameters listed in K12.

or H I dark clouds. Associated absorbers can be found in AGN outflows, circumnuclear discs, and cold gas clouds in the host galaxy or merger relics (Maccagni et al. 2017; Allison et al. 2019; Oosterloo et al. 2019). The cold molecular gas in these systems is not well studied due to a low detection number (Allison et al. 2019) and they could potentially have very different OH column densities and different excitation temperatures (Curran et al. 2016). Therefore, we observe a sample of low-redshift ($z<0.3$) galaxies with associated H I 21-cm absorption detections, with an extra target with a deep intervening H I 21-cm absorption for comparison, using the Five-hundred-meter Aperture Spherical radio Telescope (FAST; Nan et al. 2011; Li & Pan 2016; Li et al. 2018a; Jiang et al. 2020) aiming to study their cold gas parameters through OH absorptions.

The outline of the paper is as follows: we describe the sample and observation strategy in Section 2; we then present the data reduction procedure and standing wave removal algorithm in Section 3; we show our results and discussions in Section 4 and summarize them in Section 5. An H I 21-cm absorption spectrum derived from our data is shown in Appendix A.

2 SAMPLE SELECTION AND OBSERVATIONS

We use the presence of H I 21-cm absorption as a prior for there being significant column densities of (possibly cold) neutral gas in front of the radio source, which would increase our chances of detecting OH molecular absorption. We select our sample from the Westerbork Synthesis Radio Telescope (WSRT) H I absorption survey (Geréb, Morganti & Oosterloo 2014; Geréb et al. 2015; Maccagni et al. 2017), which has 64 associated H I 21-cm absorption detections in total and 14 of them have their OH 18-cm main lines (1665 and 1667 MHz) that fall within the FAST frequency ranges. We observed eight of them in this pilot project. A target with a deep intervening absorption selected from Dutta et al. (2017) is also observed for comparison. Parameters of the targets are listed in Table 2.

FAST has finished its construction and is now taking observations (Jiang et al. 2020). Its declination range is from −14.3 to +65.7 deg, and −0.7 to +52.1 deg for full sensitivity. The potential of FAST for extragalactic absorption study has been discussed by Yu et al. (2017) and Li, Dickey & Liu (2019). FAST is currently mounted with a 19-beam receiver covering 1.05– 1.45 GHz. The beam size is about 2.9" and the system temperature around 1.4 GHz is less than 24 K for the central beam. The spectral back-end can record data in four polarizations with a frequency resolution of about 7.63 kHz (65 536 channels over 1.0–1.5 GHz).

This paper is based on data from a 'Shared-Risk' pilot observation program. The initial part of the observation for SDSS J084307.11+453742.8 was taken in normal tracking mode. We use the central beam (M01) of the 19-beam receiver to track the target for 2 min and then move the beam towards an OFF point for 2 min. The switch time between ON and OFF points is about 10 min. Later observations for other sources were taken in a newly developed ON–OFF mode. The ON–OFF mode has a much shorter ON–OFF switch time, i.e. 30 s, if the distance between ON and OFF points is within 30 arcmin. We have carefully chosen the OFF point for each source so that a side beam (M08 or M14) would be pointing to the source when the central beam is pointing to the OFF point. We do multiple ON–OFF cycles for each source and the ON-source integration time for each cycle is 2–3 min. The total (including central beam and side beam) integration time for each source is tabulated in Table 3.

We record the data every 0.1 s. For most of the observations, we inject a 10 K continuum signal using a noise diode for 0.1 s every 1 s. For SDSS J205449.64+004149.8, we inject the noise for 1 s every 3 min.

3 DATA REDUCTION AND STANDING WAVE REMOVAL

We extract the noise diode signals from the data and use them to convert the spectral signals without noise diode injections into units of K. Obvious radio frequency interference (RFI) is removed using a 3σ clipping method. We then do ON–OFF subtraction and combine the first two polarizations. The results are shown in Fig. 1. The spectra are normalized by dividing a straight line fitted using the continuum around the OH 1667 line vicinity.

Some of the spectra are affected by standing waves with a frequency of about 1 MHz, which corresponds to a velocity width

Table 2. Targets observed with FAST.

Source name	RA (deg) (1)	Dec (deg) (2)	z_{opt} (3)	$S_{1.4\,GHz}$ (mJy) (4)	$\log P_{1.4\,GHz}$ ($W\,Hz^{-1}$) (5)	Type (6)	$\tau_{H\,I,\,peak}$ (7)	$\int \tau_{H\,I}\,dv$ ($km\,s^{-1}$) (8)	H I FWHM ($km\,s^{-1}$) (9)	$v_{H\,I}$ ($km\,s^{-1}$) (10)
J084307.11+453742.8	130.77962	+45.62856	0.1919	331.00	25.54	A	0.2730	25.86	79.2	57.85
J112332.04+235047.8	170.88350	+23.84661	0.2070	142.69	25.25	A	0.1048	5.01	156.2	219.69
J170815.25+211117.7	257.06354	+21.18825	0.2241	34.36	24.71	A	0.1569	28.38	211.1	3.23
J130132.61+463402.7	195.38587	+46.56742	0.2055	97.00	25.07	A	0.0180	4.24	172.4	− 308.84
J142210.81+210554.1	215.54504	+21.09836	0.1915	84.30	24.94	A	0.0480	8.36	179.8	− 196.05
J103932.12+461205.3	159.88383	+46.20147	0.1861	30.81	24.48	A	0.0859	14.75	86.1	3.23
J153452.95+290919.8	233.72062	+29.15550	0.2010	48.57	24.75	A	0.0275	6.77	233.7	26.61
J090325.54+162256.0	135.85642	+16.38222	0.1823	47.81	24.65	A	0.0949	8.98	163.0	2.97
J205449.64+004149.8[a]	313.70685	+0.69718	0.2015	362.00	25.55	I	0.61	29.92	150.0	–

Notes. Columns: (1) hour angle in degree; (2) declination in degree; (3) optical redshift from SDSS; (4) 1.4 GHz continuum flux of the quasar in mJy; (5) 1.4 GHz continuum flux of the quasar in physical units; (6) type of the absorber, A for associated, I for intervening; (7) peak H I optical depth; (8) integrated H I optical depth; (9) FWHM of the H I 21-cm absorption; and (10) H I 21-cm absorption centroid velocity from the optical redshift.
Notes: (*a*) SDSS J205449.64+004149.8 is a QSO–galaxy pair (QGP) with the QSO redshift $z = 0.284$ (Dutta et al. 2017). Other targets are selected from Maccagni et al. (2017).

Table 3. Optical depth upper limits of FAST spectra.

Source name	t_{int} (min) (1)	$\tau_{1667,rms}$ (10^{-2}) (2)	Velocity resolution ($km\,s^{-1}$) (3)	$3\int \tau_{1667,\,rms}\,dv$ ($km\,s^{-1}$) (4)
J084307.11+453742.8	30	0.21	1.64	0.07
J112332.04+235047.8	19	0.51	1.66	0.25
J170815.25+211117.7	24	2.81	1.68	1.59
J130132.61+463402.7	24	0.50	1.65	0.25
J142210.81+210554.1	24	0.61	1.64	0.31
J103932.12+461205.3	22	0.31	1.63	0.11
J153452.95+290919.8	23	1.02	1.65	0.60
J090325.54+162256.0	16	1.79	1.62	0.87
J205449.64+004149.8	132	0.06	1.65	0.03

Note. Columns: (1) On-target integration time. (2) rms of the normalized spectra after standing wave removal around the OH 1667 line (within 1 MHz). (3) Velocity resolution around the observed frequency of OH 1667 line. (4) 3σ upper limit of integrated OH 1667 optical depth within H I FWHM.

of about 200 $km\,s^{-1}$ at 1600 MHz. This 1 MHz standing wave could be introduced by reflections of leaked signals between the receiver and the bottom panel of the telescope. Improvements in hardware have been made to reduce the reflections but the standing wave still exists. We thus remove these 1 MHz ripples using the following prescription. (1) Shape of the ripple is relatively stable in spectra taken within one observation cycle (2–3 min). So we do Fourier transform on the original spectrum from each observation cycle and identify the peak location t_p within 0.91 and 0.95 μs. (2) We smooth the spectrum using a Gaussian kernel and subtract the smoothed spectrum from the original spectrum. The width (standard deviation) of the Gaussian kernel is chosen to be 60 channels (about 0.46 MHz) so that the smoothed curve is free of the 1 MHz ripple but still retains features with widths larger than 1 MHz. (3) We fit the resulting spectrum (excluding the 1 MHz region around the OH 1667 MHz line) using a sinusoidal function with a fixed period of $1/t_p$. (4) We then obtain the ripple removed spectrum by subtracting the fitted sinusoidal function from the original spectrum. An example of this fitting process is shown in Fig. 2.

4 RESULTS AND DISCUSSIONS

The final reduced spectra with standing waves removed are shown in Fig. 3. The locations of the redshifted OH 1665 and 1667 lines are marked by red vertical dash lines. Note that the dips around the vertical lines can be attributed to RFI. We do not see any robust OH absorption signal. The rms values around the OH 1667 line are also shown in each panel. Five sources are affected by RFI, while the remaining four are relatively clean. The derived 3σ integrated optical depth upper-limits range from 0.03 to 1.6, assuming the H I line width. The extremely low limit of 0.03 resulted from a 2-h integration toward J205449.64+004149.8. Observation details and rms values are also tabulated in Table 3.

We plot the integrated H I optical depth versus integrated OH 1667 optical depth in the left-hand panel of Fig. 4, together with detections and upper limits from Gupta et al. (2018). We show linear fits to both associated and intervening absorbers using a survival statistics (Feigelson & Nelson 1985) with the Schmitt binning method (Schmitt 1985), which can deal with detections and upper limits simultaneously. The fitted relation for the associated absorbers is $\log \int \tau_{1667} dv = (-\,1.86 \pm 0.64) + (1.21 \pm 0.61) \times \log \int \tau_{H\,I} dv$, with the generalized Spearman's correlation parameter $\rho = 0.17$ and a probability of 60 per cent for a null correlation. The fitted relation for the intervening absorbers is $\log \int \tau_{1667} dv = (-\,1.18 \pm 0.20) + (0.91 \pm 0.30) \times \log \int \tau_{H\,I} dv$, with $\rho = 0.28$ and a probability of 33 per cent for a null correlation. Both associated and intervening absorbers show a weak positive correlation between integrated H I and OH optical depths from the fitting, however, the fitting uncertainties are large and the statistics may not be reliable because of small sample numbers, especially for the associated

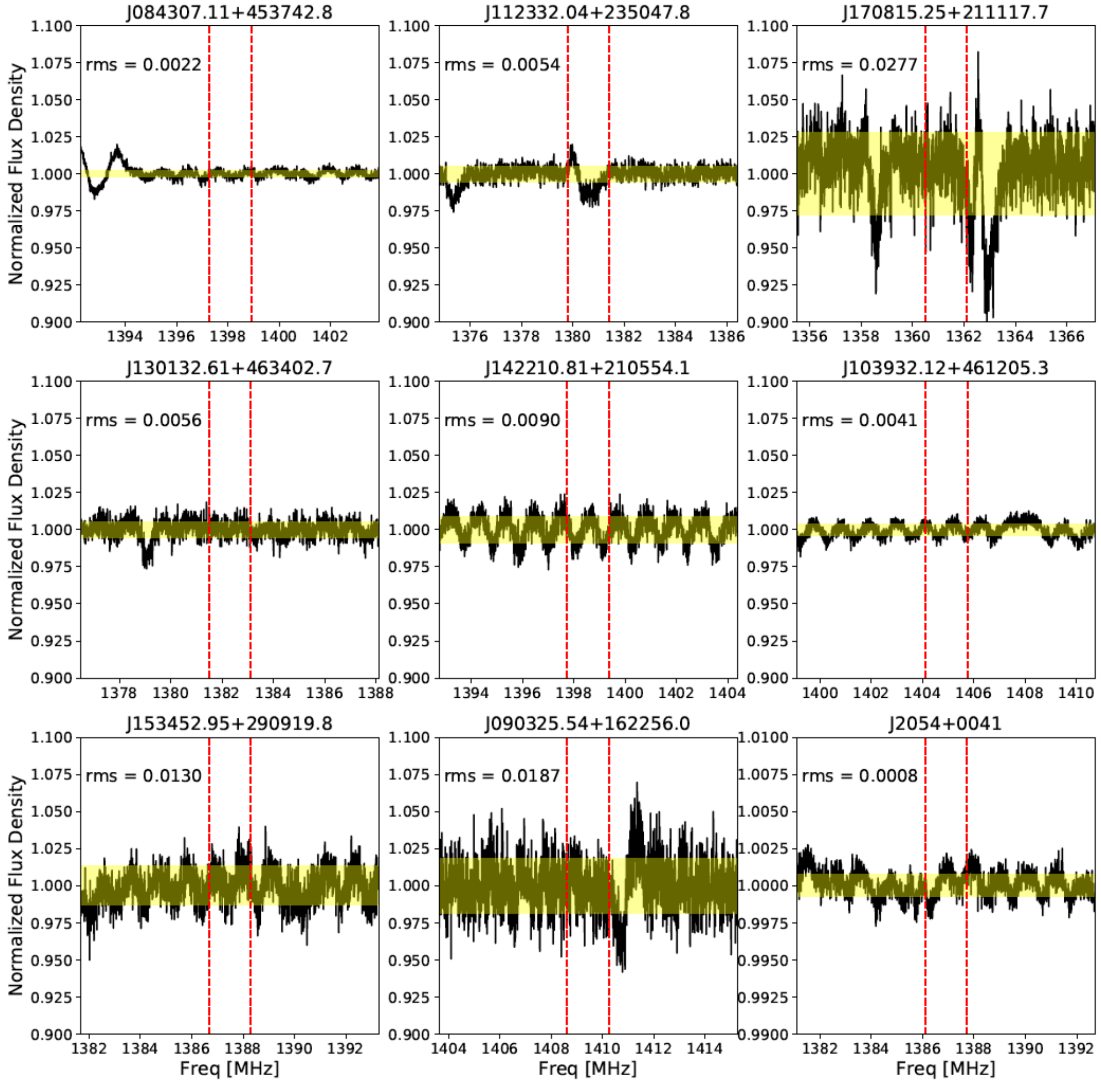

Figure 1. Initial spectra of the targets before removal of the baseline ripple. The red vertical dash lines show the expected locations of redshifted OH 1665 and 1667 lines, calculated from the optical redshifts and H I 21-cm absorption velocities. The rms values of the spectra within the shown frequency range are shown in each panel. A yellow shaded region is also overplotted in each panel to show the rms. Note the last panel (J2054+0041) has a much smaller *y*-axis range.

absorbers. The associated absorbers generally have lower OH optical depths than intervening absorbers with similar H I optical depths: the mean integrated OH 1667 optical depth of the detected intervening and associated absorbers are 1.13 and 0.24, respectively.

We calculate the H I and OH column densities using

$$\mathrm{N(H\,I)} = 1.823 \times 10^{18}\,\frac{T_x^{\mathrm{HI}}}{f_{\mathrm{c}}^{\mathrm{HI}}}\int \tau_{\mathrm{HI}}\mathrm{d}v\ \mathrm{cm}^{-2}, \quad (1)$$

and

$$\mathrm{N(OH)} = 2.24 \times 10^{14}\,\frac{T_x^{\mathrm{OH}}}{f_{\mathrm{c}}^{\mathrm{OH}}}\int \tau_{1667}\mathrm{d}v\ \mathrm{cm}^{-2}, \quad (2)$$

where T_x^{HI} and T_x^{OH} are excitation temperatures and $f_{\mathrm{c}}^{\mathrm{HI}}$ and $f_{\mathrm{c}}^{\mathrm{OH}}$ covering factors of H I and OH. We use $T_x^{\mathrm{HI}} = 100$ K, $T_x^{\mathrm{OH}} = 10$ K, $f_{\mathrm{c}}^{\mathrm{HI}} = 1$, and $f_{\mathrm{c}}^{\mathrm{OH}} = 1$ for all our targets, which are generally used in most previously detected absorbers at cosmological distances (e.g. Kanekar & Chengalur 2002; Grasha et al. 2019). We plot the column densities in the right-hand panel of Fig. 4. Gupta et al. (2018) claim that their OH column densities are much lower than previously detected OH absorbers but we see no gap between the upper limits and detections. Note they assume the OH velocity widths are 2 km s^{-1} and the OH excitation temperature $T_x^{\mathrm{OH}} = 3.5$ K. Here, we assume the velocity widths of the OH 1667 lines are the same as their H I 21-cm absorption lines and $T_x^{\mathrm{OH}} = 10$ K, $f_{\mathrm{c}}^{\mathrm{OH}} = 1$. We also perform survival statistical analysis to the H I and OH column densities. The fitted relation for the associated absorbers is $\log \mathrm{N(OH)} = (-5.97 \pm 5.61) + (0.97 \pm 0.27) \times \log \mathrm{N(H\,I)}$, with the generalized Spearman's correlation parameter $\rho = 0.68$ and a probability of 4 per cent for a null correlation. The fitted relation for the intervening absorbers is $\log \mathrm{N(OH)} = (-8.17 \pm 6.16) + (1.09 \pm 0.30) \times \log \mathrm{N(H\,I)}$, with $\rho = 0.12$ and a probability of 67 per cent for a null correlation. They are consistent with the relationship between the integrated H I and OH optical depths.

We explore the evolution of OH abundance by plotting the OH/H I optical depth and column density ratios versus redshift in Fig. 5. Although we show in Fig. 4 that the gap between OH column densities calculated by Gupta et al. (2018) and previous high redshift detections disappeared if using a uniform T_x^{OH} and a wider velocity

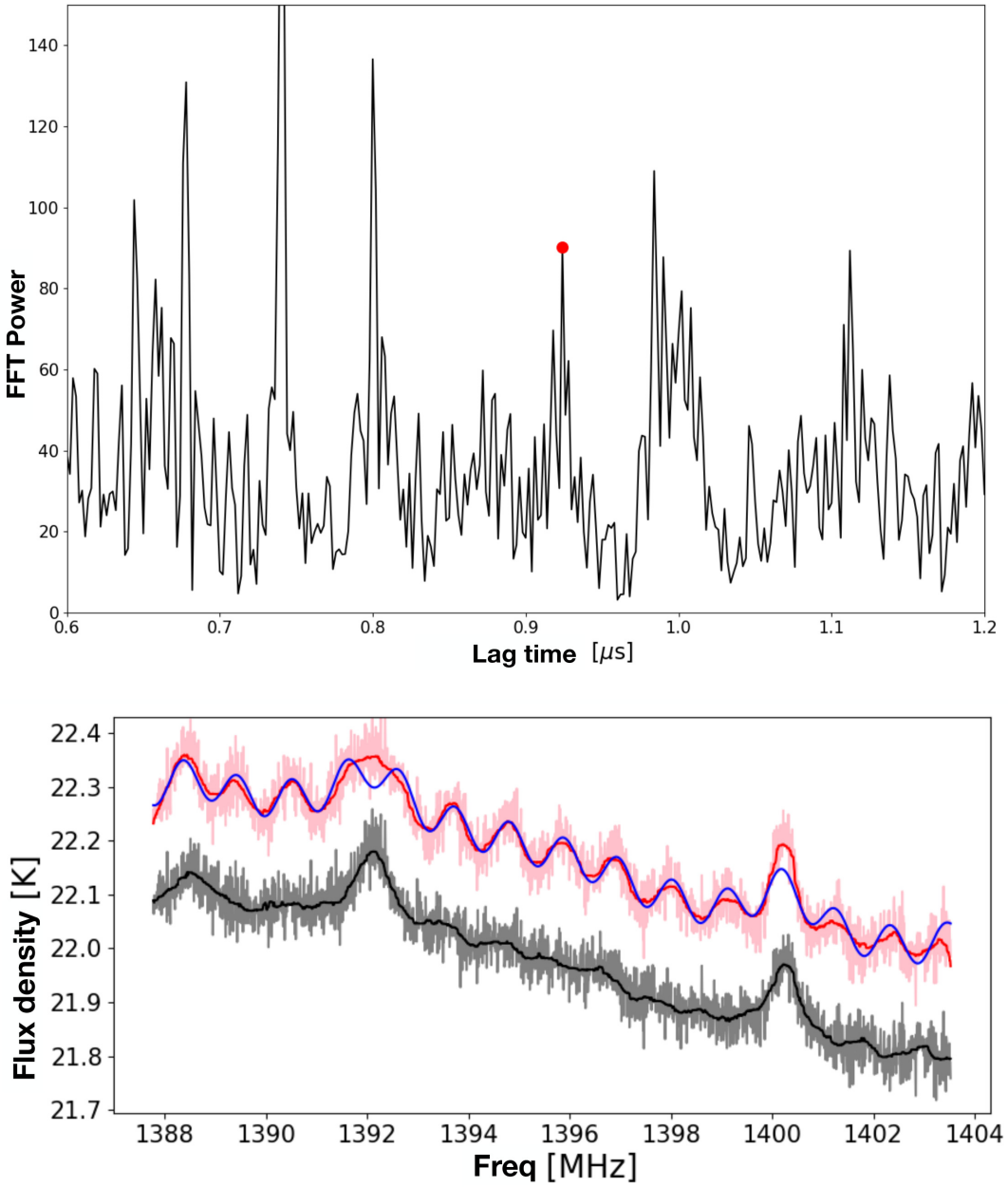

Figure 2. Example of standing wave removal. Upper panel shows the Fourier transform of a spectrum. The red dot indicates the location of the 1 MHz standing wave. Lower panel shows the spectrum before (pink) and after (grey) ripple removal. The blue line shows the sinusoidal fitting on top of the Gaussian smoothed spectrum. The red and black lines show the median filtered spectra with a filter window of 53 channel (0.4 MHz). The ripple removed spectrum is shifted down by 0.2 K in this plot for a better view.

width, Fig. 5 shows that absorbers with a redshift less than 0.4 still have a lower OH/H I column density ratio than those with a higher redshift. The linear fitting using the survival statistics show that both associated and intervening absorbers have an increasing OH abundance with increasing redshift. The fitted relations for the associated absorbers are $\log \int \tau_{1667} \mathrm{d}v / \int \tau_{\mathrm{H\,I}} \mathrm{d}v = (-2.32 \pm 1.66) + (1.71 \pm 7.79) \times z$, and $\log \mathrm{N(OH)/N(H\,I)} = (-7.32 \pm 1.39) + (2.21 \pm 6.36) \times z$; and the generalized Spearman's $\rho = 0.57$ and 0.56, and a null correlation probability of 9 per cent and 5 per cent, respectively. The fitted relations for the intervening absorbers are $\log \int \tau_{1667} \mathrm{d}v / \int \tau_{\mathrm{H\,I}} \mathrm{d}v = (-1.76 \pm 0.29) + (1.96 \pm 0.62)\, z$, and $\log \mathrm{N(OH)/N(H\,I)} = (-6.80 \pm 0.24) + (2.14 \pm 0.43)\, z$; with $\rho = 0.57$ and 0.65, and a null correlation probability of 9 per cent and 2 per cent, respectively. This implies that the molecular fraction has decreased from higher redshifts down to $z < 0.4$ and this could be the reason of the star formation rate decline since $z = 2$ (Madau & Dickinson 2014). It is consistent with previous studies such as Tacconi et al. (2020, and references therein), which show that the CO traced molecular gas content decreased since redshift ∼1.4. However, we note that OH is a tracer of diffuse molecular gas, as opposed to CO being a more direct tracer of dense molecular clouds and star formation (e.g. van Dishoeck & Black 1986; Allen et al. 2015; Xu et al. 2016).

Figs 4–5 show that most associated absorbers have a lower OH abundance comparing to intervening absorbers. Curran et al. (2016) claim that associated absorbers are mostly originated from high-

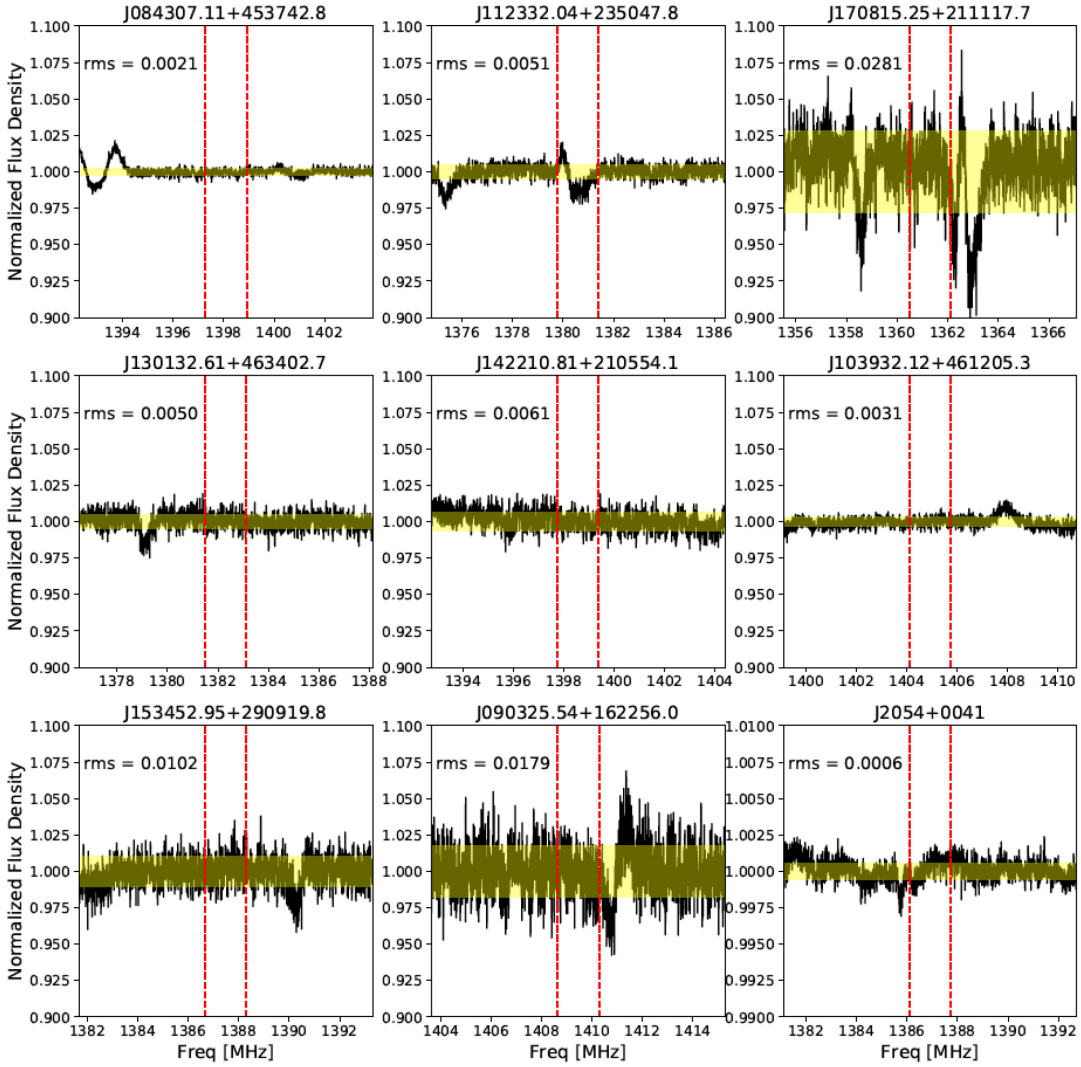

Figure 3. Final spectra, as in Fig. 1 but with the baseline ripple removed. Note that the dips in these panels are all caused by RFI.

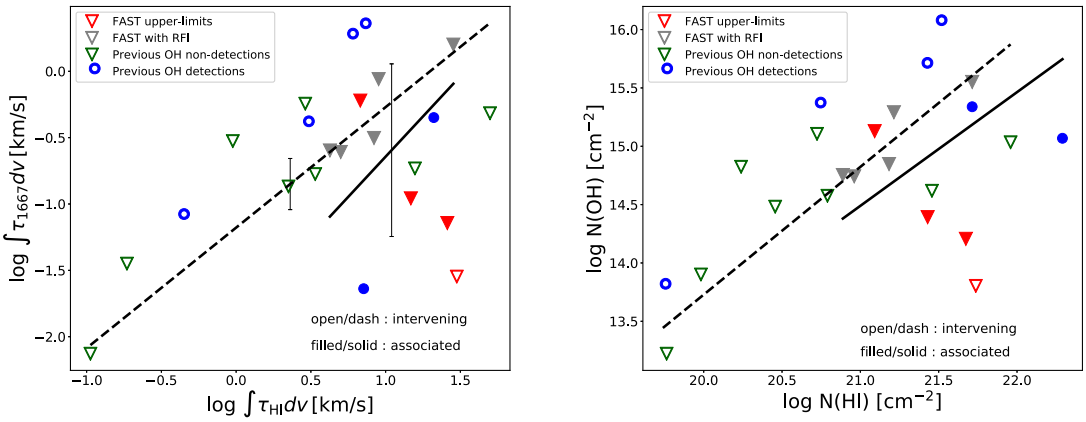

Figure 4. Left-hand panel: Integrated H I optical depth versus integrated OH 1667 optical depth; right-hand panel: H I column density versus OH column density. Red triangles are 3σ upper limits derived using newly observed FAST data, grey triangles are also upper limits from FAST data with obvious RFI, green triangles are upper limits calculated using the spectral rms and H I FWHM provided by Gupta et al. (2018) and references therein, blue dots are the six OH absorption detections listed in Table 1. Open symbols are intervening absorbers and filled symbols are associated absorbers. The black solid and dash lines show a linear fit to the associated and intervening absorbers respectively using a survival statistics (Feigelson & Nelson 1985) with the Schmitt binning method (Schmitt 1985). The 1σ uncertainties for the fittings on the y-axis are shown as error bars. We do not show the error bars for the right-hand panel because the uncertainties, 5.61 and 6.61 for the solid and dash lines, respectively, are much larger than the y-axis range shown here.

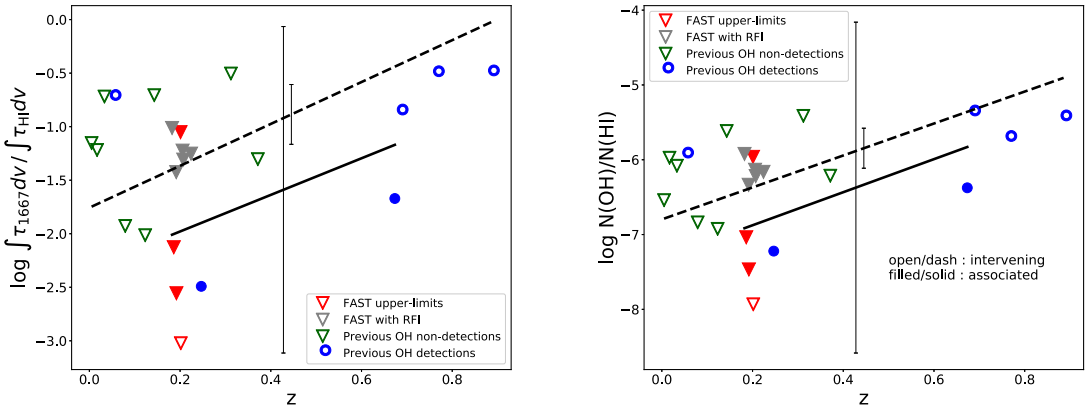

Figure 5. Integrated OH and H I optical depth ratio (left-hand panel) and OH/H I column density ratio (right-hand panel) versus redshift. Symbols are the same as Fig. 4.

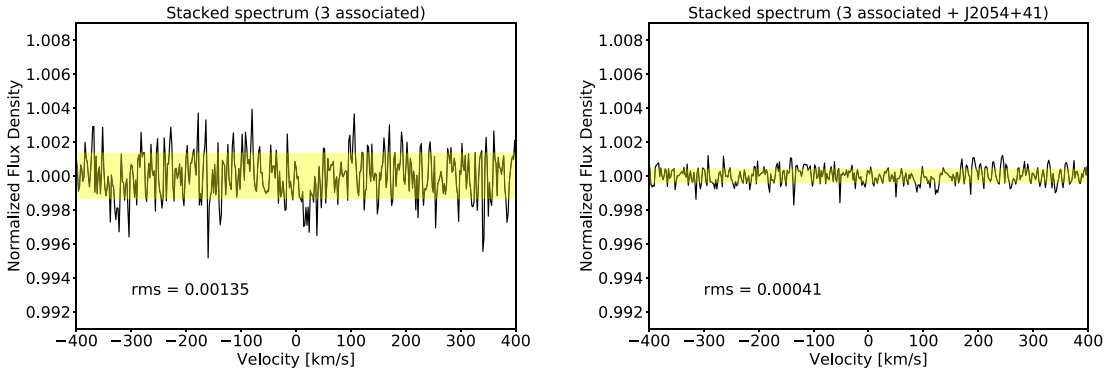

Figure 6. Stacked spectra. Left-hand panel shows the stacked spectrum of the three associated absorbers J084307.11+453742.8, J153452.95+290919.8, and J103932.12+461205.3, which are free of RFI at the vicinity of their OH 1667 lines. Right-hand panel shows the stacked spectrum of the three plus J205449.64+004149.8. The spectra are centred at the OH 1667 line and have a velocity resolution of 2 km s^{-1}. A yellow shaded region is overplotted to show the rms.

velocity nuclear gas feeding the central AGN. This implies that the AGNs in these sources are not promoting OH molecule formation if not considering the effects of covering factors and excitation temperatures.

We note that the correlations derived above using the survival statistics have large uncertainties. Furthermore, the reported generalized Spearman's correlation parameters may not be reliable because the data points used in the analysis are less than 30. We expect a further observation of at least more than 20 absorbers spanning a wider redshift range in the future in hope to reveal a more reliable relationship between OH abundance and redshifts. This could potentially provide a better constrain to the molecular abundance evolution in galaxies.

We stack the ripple removed spectra of three of our associated absorbers that are free of RFI, i.e. J084307.11+453742.8, J153452.95+290919.8, and J103932.12+461205.3. We weight each individual spectrum using their inverse variance ($1/rms^2$) during stacking. The normalized stacked spectrum is shown in the left-hand panel of Fig. 6. There is a dip in the stacked spectrum around 0 km s^{-1} but the amplitude is well within 3σ of the spectrum. The 3σ OH column density upper limit derived using the stacked spectrum rms = 0.00135, with an assumed OH velocity width of 150 km s^{-1}, $T_x^{OH} = 10$ K and $f_c^{OH} = 1$, is about 1.57×10^{14} cm^{-2}, which are consistent with previous values (Kanekar & Chengalur 2002; Kanekar et al. 2003, 2005; Gupta et al. 2018). Using a mean H I column density of the four targets, we obtain an OH abundance upper limit [OH]/[H I] $< \sim 5.45 \times 10^{-8}$ for these associated absorbers, which is only 50 per cent of the typical Galactic value (Nguyen et al. 2018) and represents the deepest extragalactic limit to the OH abundance achieved by OH absorption measurement at cosmological distances. We further added the spectrum of the intervening absorber J205449.64+004149.8 in the stacking and the result is shown in the right-hand panel of Fig. 6. The rms of the stacked spectrum, 0.00041, is then dominated by J205449.64+004149.8. We do not see any obvious OH 1667 absorption line in the stacked spectrum either.

5 SUMMARY

We derive upper limits of OH column densities for eight associated and one intervening absorbers at redshifts z∈ [0.1919,0.2241] through absorption measurements with FAST. The combined upper limits to the OH abundance for three associated absorbers, [OH]/[H I] $< \sim 5.45 \times 10^{-8}$, is the lowest ever achieved. The associated absorbers have a slightly lower OH abundance than their intervening counterparts. The results are largely consistent with a trend of decreasing OH abundance with decreasing z.

ACKNOWLEDGEMENTS

We thank Carl Heiles and Marko Krco for useful discussions. We also thank the anonymous referee for very helpful comments

and extremely efficient responses. This work was supported by the National Natural Science Foundation of China grant numbers 11988101, 11725313, U1931110, and 11703036, the International Partnership Program of Chinese Academy of Sciences grant number 114A11KYSB20160008, and the CAS Interdisciplinary Innovation Team (JCTD-2019-05). Parts of this research were supported by the Australian Research Council Centre of Excellence for All Sky Astrophysics in 3 Dimensions (ASTRO 3D), through project number CE170100013. ZZ also acknowledges support from an ACAMAR visiting fellowship.

DATA AVAILABILITY

The data underlying this article are available in the project 2019a-035-S at https://fast.bao.ac.cn/cms/article/95/, and can be shared on request to the FAST data centre or to the corresponding author.

REFERENCES

Allen R. J., Hogg D. E., Engelke P. D., 2015, AJ, 149, 123
Allison J. R., Curran S. J., Sadler E. M., Reeves S. N., 2013, MNRAS, 430, 157
Allison J. R. et al., 2017, MNRAS, 465, 4450
Allison J. R. et al., 2019, MNRAS, 482, 2934
Barkhouse W. A., Hall P. B., 2001, AJ, 121, 2843
Carilli C. L., Perlman E. S., Stocke J. T., 1992, ApJ, 400, L13
Carilli C. L., Menten K. M., Reid M. J., Rupen M. P., 1997, ApJ, 474, L89
Chengalur J. N., de Bruyn A. G., Narasimha D., 1999, A&A, 343, L79
Cohen J. G., Lawrence C. R., Blandford R. D., 2003, ApJ, 583, 67
Curran S. J., Kanekar N., Darling J. K., 2004, New Astron. Rev., 48, 1095
Curran S. J., Tanna A., Koch F. E., Berengut J. C., Webb J. K., Stark A. A., Flambaum V. V., 2011, A&A, 533, A55
Curran S. J., Duchesne S. W., Divoli A., Allison J. R., 2016, MNRAS, 462, 4197
Dutta R., Srianand R., Gupta N., Momjian E., Noterdaeme P., Petitjean P., Rahmani H., 2017, MNRAS, 465, 588
Feigelson E. D., Nelson P. I., 1985, ApJ, 293, 192
Geréb K., Morganti R., Oosterloo T., 2014, A&A, 569, A35
Geréb K., Maccagni F., Morganti R., Oosterloo T., 2015, A&A, 575, A44
Grasha K., Darling J., Bolatto A., Leroy A. K., Stocke J. T., 2019, ApJS, 245, 3
Grasha K., Darling J., Leroy A. K., Bolatto A. D., 2020, MNRAS, 498, 883
Grenier I. A., Casandjian J.-M., Terrier R., 2005, Science, 307, 1292
Gupta N., Momjian E., Srianand R., Petitjean P., Noterdaeme P., Gyanchandani D., Sharma R., Kulkarni S., 2018, ApJ, 860, L22
Gupta N. et al., 2020, preprint (arXiv:2007.04347)
Jiang P. et al., 2020, Res. Astron. Astrophys., 20, 64
Kanekar N., Briggs F. H., 2003, A&A, 412, L29
Kanekar N., Chengalur J. N., 2002, A&A, 381, L73
Kanekar N., Chengalur J. N., de Bruyn A. G., Narasimha D., 2003, MNRAS, 345, L7
Kanekar N. et al., 2005, Phys. Rev. Lett., 95, 261301
Kanekar N., Langston G. I., Stocke J. T., Carilli C. L., Menten K. M., 2012, ApJ, 746, L16
Kanekar N., Ghosh T., Chengalur J. N., 2018, Phys. Rev. Lett., 120, 061302
Li D. et al., 2018a, IEEE Microw. Mag., 19, 112
Li D. et al., 2018b, ApJS, 235, 1
Li D., Pan Z., 2016, Radio Sci., 51, 1060
Li D., Dickey J. M., Liu S., 2019, Res. Astron. Astrophys., 19, 016
Maccagni F. M., Morganti R., Oosterloo T. A., Geréb K., Maddox N., 2017, A&A, 604, A43
Madau P., Dickinson M., 2014, ARA&A, 52, 415
Nan R. et al., 2011, Int. J. Mod. Phys. D, 20, 989
Nguyen H. et al., 2018, ApJ, 862, 49
Oosterloo T., Morganti R., Tadhunter C., Raymond Oonk J. B., Bignall H. E., Tzioumis T., Reynolds C., 2019, A&A, 632, A66
Remy Q., Grenier I. A., Marshall D. J., Casand jian J. M., 2017, A&A, 601, A78
Schmitt J. H. M. M., 1985, ApJ, 293, 178
Tacconi L. J., Genzel R., Sternberg A., 2020, preprint (arXiv:2003.06245)
Turner B. E., 1979, A&AS, 37, 1
van Dishoeck E. F., Black J. H., 1986, ApJS, 62, 109
van Dishoeck E. F., Black J. H., 1988, in Millar T. J., Williams D. A., eds, Rate Coefficients in Astrochemistry. Kluwer, Dordrecht, p. 209
Weinreb S., Barrett A. H., Meeks M. L., Henry J. C., 1963, Nature, 200, 829
Wenger M. et al., 2000, A&AS, 143, 9
Xu D., Li D., Yue N., Goldsmith P. F., 2016, ApJ, 819, 22
Yu H.-R., Pen U.-L., Zhang T.-J., Li D., Chen X., 2017, Res. Astron. Astrophys., 17, 049

APPENDIX A: H I 21-CM ABSORPTION OF J084307.11+453742.8

Although most of the H I frequencies of our targets locate within the 1150–1250 MHz frequency range, which is severally affected by satellite RFI, one of our targets, J084307.11+453742.8, does show a deep H I 21-cm absorption. The H I absorption feature is shown in Fig. A1. The integrated optical depth from -200 to 200 km s^{-1} is about 29.79 km s^{-1}, which is a little bit larger than the value from Maccagni et al. (2017) (Table 2). We fit the absorption profile with two Gaussian components and the resulting peak optical depths and FWHMs are $\tau_{p1} = 0.58$, FWHM$_1$ = 23.83 km s^{-1}, $\tau_{p2} = 0.18$, FWHM$_2$ = 78.13 km s^{-1}. The narrow component has a much deeper and narrower absorption profile comparing to Maccagni et al. (2017). A possible explanation for the difference could be that an extra compact component with a proper motion moving into the line of sight. However, it could also be due to measurement error or scattering of the absorbing region due to the ISM in either the host galaxy or the Milky Way.

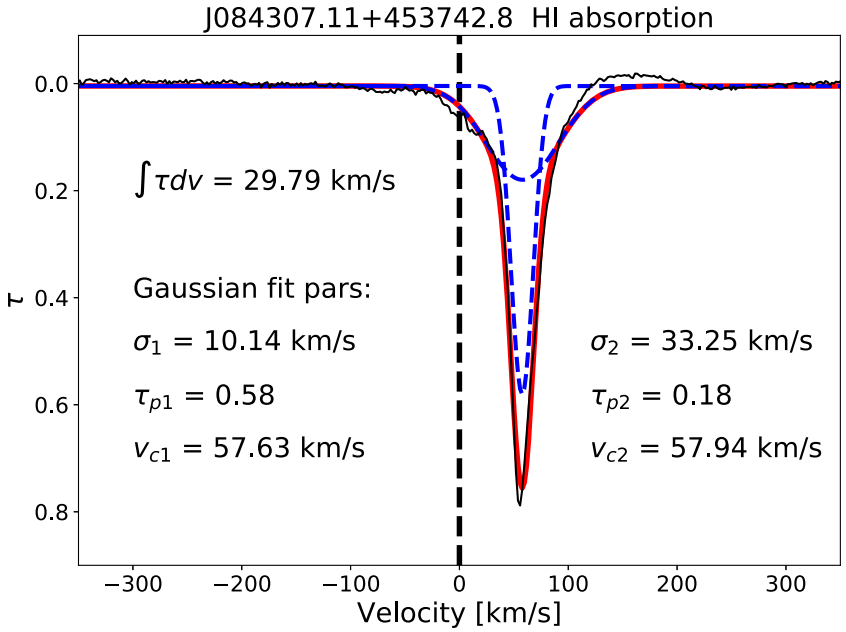

Figure A1. FAST H I 21-cm absorption spectrum of J084307.11+453742.8. The blue dash lines show the two fitted Gaussian components, the red line shows the combined fit, and the vertical dash line shows the optical velocity of the target.

This paper has been typeset from a TEX/LATEX file prepared by the author.